

Dislocation Avalanches: Earthquakes on the Micron Scale

Péter Dusán Ispánovity^{a,*}, Dávid Ugi^a, Gábor Péterffy^a, Michal Knapek^b, Szilvia Kalácska^a, Dániel Tüzes^a, Zoltán Dankházi^a, Kristián Máthis^b, František Chmelík^b, István Groma^a

^a*Eötvös Loránd University, Department of Materials Physics, 1117 Budapest, Pázmány Péter sétány 1/a. Hungary*

^b*Charles University, Faculty of Physics of Materials, Department of Physics of Materials, 121 16 Prague 2, Ke Karlovu 5, Czech Republic*

Abstract

Metals usually deform irreversibly as a result of the motion of dislocations that are line-like defects in the crystal lattice. Compression experiments of micron-scale specimens^{1,2} as well as acoustic emission (AE) measurements performed on bulk samples^{3,4} revealed that the motion of dislocations resembles a stick-slip process. As a result, deformation proceeds in a series of unpredictable local strain bursts with a scale-free size distribution^{5,6}. Here we use a unique, highly sensitive experimental set-up, which allows us to detect the weak AE waves of dislocation slip during the compression of micron-sized Zn pillars. This opens up new vistas for studying the stop-and-go dislocation motion in detail and understanding the physical origin of AE events. Profound correlation is observed between the size of the deformation events and the total energy of the emitted signals that, as we conclude, are induced by the collective dissipative motion of dislocations. We also show by statistical

*Corresponding author

Email address: ispanovity@metal.elte.hu (Péter Dusán Ispánovity)

analyses of the acoustic event sequences that, despite of the fundamental differences in the deformation mechanism and the huge gap in the involved length and timescales, dislocation avalanches and earthquakes are essentially alike. Our experimental and computer simulation results not only unveil the complex spatiotemporal structure of strain bursts but also exhibit technological importance by unraveling the missing relationship between the properties of acoustic signals and the corresponding local deformation events.

Keywords: Crystal plasticity, dislocation avalanche, strain burst, micromechanics, acoustic emission

1 It was not until 1934 that the basic mechanism of irreversible (or plastic) de-
2 formation of metals was finally understood when Orowan, Taylor and Polányi
3 independently postulated the existence of a specific lattice defect^{7,8,9}. These
4 line-like defects, called dislocations, can move within the crystal lattice lead-
5 ing to the rearrangement of the atoms and, as a consequence, to the plas-
6 tic shear deformation of the crystal. Due to the huge dislocation content in
7 macroscopic metallic samples, their deformation usually appears as a smooth
8 process both in space and time. On microscopic scales, however, the picture
9 changes dramatically. Recent micromechanical experiments demonstrated
10 that when the sample diameter is below several couples of μm (depending on
11 the material), deformation becomes strongly heterogeneous. As pioneering
12 compression tests on Ni single crystal *micropillars* prepared using focused
13 ion beam (FIB) milling revealed, deformation is a sequence of sudden unpre-
14 dictable strain bursts that are localized to specific crystallographic planes of
15 the sample^{1,2}. During these intermittent bursts, dislocations locally disen-
16 tangle and move quickly for a short period and then form novel metastable

17 sub-structures at the end of an event. The burst sizes follow a scale-free
18 distribution that suggests an underlying self-organization of the dislocation
19 structure upon these plastic events^{5,6}.

20 A unique experimental method that is able to monitor this stochastic
21 response is the detection of AE waves. The principle of the emission of
22 acoustic waves in materials is analogous to earthquakes: Plastic deformation
23 is caused by the local rearrangement of dislocation lines in a crystal, a process
24 that is strongly dissipative and part of the released elastic energy escapes in
25 the form of elastic waves, that can be detected at the surface¹⁰. It was found
26 that in bulk single crystals the recorded AE signal is burst-like and the energy
27 associated with individual bursts follows a scale-free distribution^{3,4}. The
28 found power-law exponent is robust, typically not affected by deformation
29 mode, and for single crystals with hexagonal closed-packed (HCP) structure
30 it was measured to be $\tau_E = 1.5 \pm 0.1$ ¹¹. These kinds of measurements so
31 far have only been performed on bulk samples and it is believed – but not
32 yet demonstrated – that the AE waves are emitted from similar local strain
33 events that can be directly observed only for micron-scale objects.

34 One of the foremost achievements of this work is the realization of the
35 nontrivial task of detecting extremely weak AE waves which arise during
36 micropillar deformation. The main advantage of this approach is that, in
37 this case, AE sources are highly localized within a small micropillar volume
38 that prevents uneven attenuation of AE waves arising in different parts of
39 the specimen, this being inherent to bulk materials testing. Hence, plenty of
40 innate AE waves can be detected due to dislocation slip, which can, in turn,
41 provide interesting insights into the dynamics of plastic events. To achieve

42 this goal, the experimental set-up sketched in Fig. 1a was developed (see
43 Extended Data Fig. 1 for a photo). The device can be placed inside a scanning
44 electron microscope (SEM) that allows us to collect three different types of
45 information simultaneously during compression of the micropillars: (i) stress
46 and strain using a capacitive displacement sensor measuring the elongation
47 of a spring, (ii) acoustic signal from a piezoelectric transducer and (iii) visual
48 images using the electron beam of the SEM. The major difficulties for AE
49 detection in micropillars comprised the relatively low number of dislocations
50 involved in the slip process (compared to bulk materials testing) and various
51 sources of noise signals in the SEM chamber, mostly of electromagnetic origin.
52 For further details on the experimental set-up and remedies to these issues
53 see Methods.

54 Firstly, rectangular micropillars with a 3:1:1 aspect ratio and side lengths
55 of $d = 8 - 32 \mu\text{m}$ were prepared from a Zn single crystal oriented for single
56 slip (for more details on the sample see Methods). In Fig. 1b a micropillar
57 during the course of the experiment is shown. One can observe that dislo-
58 cation slip indeed takes place solely on the basal plane of the HCP lattice
59 (see also Supplementary Video 1). Since the crystal orientation in the pillar
60 remains the same throughout the entire loading (see Extended Data Fig. 2)
61 only dislocation glide is operative and deformation due to twinning can be
62 excluded.

63 Figure 1c plots the measured compressive stress σ as a function of time
64 t for the micropillar with $d = 32 \mu\text{m}$ shown in Fig. 1b (see also Supplemen-
65 tary Video 1). The pronounced, close-to-vertical drops correspond to the
66 strain bursts that lead to the sudden elongation of the spring of the device.

67 To analyse the spatial distribution of a strain burst two consecutive SEM
68 images taken before and after the stress drop highlighted with grey color in
69 Fig. 1c were compared with edge detection on the differential image and we
70 concluded that deformation took place solely in a thin slip band highlighted
71 with red in Fig. 1b. During the compression, AE signal is also recorded that
72 comprises numerous individual bursts and their rate exhibits robust corre-
73 lation with the stress drops (Fig. 1c). To elaborate further on this finding
74 Figs. 1d and 1e plot consecutively zoomed parts of the stress-time curve
75 shaded with grey colour. According to Fig. 1d AE events can only be de-
76 tected when plasticity occurs, that is, when the stress-time curve deviates
77 from the linear ramp-up characteristic of purely elastic deformation. Interest-
78 ingly, it is possible that several AE events correspond to the same stress drop
79 as also indicated by the event count number (Fig. 1d). The reason for this
80 is that the data acquisition rate differs considerably between stress (200 Hz)
81 and AE (2.5 MHz) measurements, the latter allowing for a more detailed
82 analysis. Figure 1e shows that the AE signal consists of short ($\lesssim 100$ μ s)
83 peaks standing out from the background noise. We, thus, conclude that the
84 AE events are indeed due to the dislocation activity leading to plastic slip
85 within the micropillar, however, the abundance of AE events suggests that a
86 measured stress drop is a result of complex internal dynamics on timescales
87 not accessible by stress measurements.

88 **Origin of AE events**

89 To quantify the correlation between plastic deformation and AE we now
90 turn to the statistical analyses of the measured data. In agreement with

91 studies on other single crystalline micropillars the distribution of the size of
 92 the individual stress drops $\Delta\sigma$ follows a scale-free distribution with a cut-off
 93 σ_0 : $P(\Delta\sigma) \propto \Delta\sigma^{-\tau_\sigma} \exp(-\Delta\sigma/\sigma_0)$ (Fig. 2a)^{5,6}. According to the inset, if the
 94 axes are re-scaled with the cross section $A = d^2$ of the micropillars (that is,
 95 force drop $\Delta F = A\Delta\sigma$ is considered as variable) the curves overlap and can
 96 be fitted with a master function yielding $\tau_\sigma = 1.8 \pm 0.1$ and $F_0 = 1.5 \pm 0.1$ mN
 97 for the exponent and the cutoff, respectively. Note that noise of the stress
 98 measurement prohibits the reliable detection of drops below ~ 0.1 mN. The
 99 distribution of the AE event energy E is characterized by another scale-free
 100 distribution now without an apparent cut-off and dependence on pillar size:
 101 $P(E) \propto E^{-\tau_E}$ (Fig. 2b) with $\tau_E = 1.7 \pm 0.1$. Note that the recorded AE
 102 events were, in general, well-defined in time, with no significant effect of
 103 signal overlapping or reflections (see Methods), as often observed in bulk
 104 samples.

105 The facts that (i) stress drops $\Delta\sigma$ and AE energies E are detected in
 106 a correlated manner, (ii) both obey a scale-free distribution and (iii) the
 107 exponents are relatively close to each other suggest that there is a physical
 108 relation between them. To shed light on such a link, Fig. 2c provides a scatter
 109 plot of $\Delta\sigma$ and E corresponding to the individual stress drops (given that at
 110 least one AE event was detected during the stress drop) for $d = 32$ μm pillars
 111 (for smaller pillar sizes see Extended Data Fig. 3). As said above, several AE
 112 events may be detected during a single drop. In such cases the energies of the
 113 corresponding AE events are added. As seen, there is a large scatter between
 114 $\Delta\sigma$ and E but, clearly, larger stress drops tend to emit signals with larger
 115 energies also expressed by the Pearson correlation found to be 0.5 ± 0.1 . If one,

116 however, bins the data with respect to the stress drop size a clear power-law
 117 relation $E \propto \Delta\sigma^\eta$ is obtained between the two quantities with $\eta = 1.2 \pm 0.2$.
 118 This can be rationalized by assuming $P(E)dE = P(\Delta\sigma)d\Delta\sigma$ yielding the
 119 relation $\eta = (\tau_\sigma - 1)/(\tau_E - 1)$ which is fulfilled by the measured exponents
 120 within error margins. This means that although a one-to-one correspondence
 121 between E and $\Delta\sigma$ does not exist, there is a close to linear relationship in the
 122 average sense that allows one to obtain the distribution of the stress drops
 123 (that are proportional to the plastic strain induced by the local deformation
 124 event) from the statistics of the AE events.

125 **Aftershock and foreshock statistics**

126 As mentioned above, AE signals emitted by local plastic deformation events
 127 are similar to elastic waves caused by the seismic activity in the Earth's
 128 crust (although they differ in their amplitude and frequency spectra by sev-
 129 eral orders of magnitude). To deepen the analogy, we now continue with the
 130 analysis of AE signals that offer a much better time resolution than the stress
 131 measurements. We intend to assess whether the AE bursts obey the three
 132 ubiquitous fundamental scaling laws associated with earthquakes. (i) The
 133 Gutenberg-Richter law¹² states that the probability density of an earthquake
 134 with released energy E decays as a power-law¹³: $P(E) \propto E^{-w}$ with $w \approx 5/3$.
 135 (ii) According to the Omori law, the rate of aftershocks r_{as} after a main shock
 136 decays approximately inversely with the time t elapsed^{14,15}: $r_{\text{as}}(t) \propto t^{-p}$ with
 137 $p \approx 1$. (iii) The 'aftershock productivity' law in seismology concludes that
 138 main shocks with larger energy E_{ms} produce on average more aftershocks:
 139 $r_{\text{as}} \propto E_{\text{ms}}^{2\alpha/3}$ with $\alpha \approx 0.8$ found empirically¹⁶. The existence of scale in-

140 variance through these power-law relationships has also been demonstrated
141 in laboratory-scale compression experiments on porous bulk materials¹⁷ and
142 rocks¹⁸.

143 It is found by our analysis that, despite the huge difference in spatial and
144 temporal scales, the deformation mechanisms and the mode of loading, all
145 three scaling laws are found to hold for micropillars, too. The Gutenberg-
146 Richter law was demonstrated in Fig. 2b and Fig. 3a proves the Omori law
147 for $d = 32 \mu\text{m}$ pillars. The line colours refer to the energy of the main shock,
148 and it is clear that the rate indeed decays as a power-law with $p = 1.1 \pm 0.1$
149 for approx. three decades and then saturates likely due to the onset of novel
150 sequences. In accordance with the productivity law the rate is larger for
151 larger main shocks and collapse can be obtained by re-scaling the rate with
152 $E_{\text{ms}}^{0.5}$ (Fig. 3b), yielding $\alpha = 0.75$. As a further proof of equivalence, Fig. 3c
153 plots the correspondent of the ‘inverse Omori law’ describing the power-law
154 increase in the rate of foreshocks r_{fs} before a main shock¹⁹. (Extended Data
155 Fig. 4 shows the corresponding figures for smaller pillars.)

156 The distribution of waiting times t_w between subsequent AE events, a key
157 measure of temporal correlations and clustering in temporal processes^{20,21},
158 was also analysed. For earthquakes a universal gamma distribution upon
159 re-scaling with the seismic occurrence rate was reported²². A similar distri-
160 bution is found here (Fig. 3d): $P(t_w) = [At_w^{-(1-\gamma)} + B] \exp(-t_w/t_0)$, which
161 can be interpreted as follows. The power-law decay for small ($\lesssim 0.1$ s) wait-
162 ing times corresponds to the correlated temporal clusters originating from
163 the same plastic event, often observed as a single stress drop. The exponent
164 $1 - \gamma = 1.2 \pm 0.1$ coincides with the Omori exponent p within error margins,

165 as expected. For larger times a plateau with an exponential cut-off is ob-
 166 served corresponding to a Poisson-like process of uncorrelated signals coming
 167 from different plastic events. To confirm this hypothesis we repeated the ex-
 168 periments for the $d = 8 \text{ }\mu\text{m}$ pillars with different platen velocities v_p (i.e.,
 169 deformation rates). Whereas the single event dynamics (power-law part) is
 170 unaffected by the velocity v_p (Fig. 3e), the collapse of the curves in the cut-off
 171 region after re-scaling the axes with the velocity v_p (Fig. 3f) yields $t_0 \propto v_p^{-1}$
 172 and $B \propto v_p$.

173 Numerical modelling

174 To provide a possible physical explanation for the experimentally observed
 175 behaviour we conduct discrete dislocation dynamics (DDD) simulations of
 176 parallel straight edge dislocations gliding on a single glide plane (see sketch
 177 in Fig. 4a). Deformation of Zn micropillars is predominantly single slip,
 178 yet, the computational model is a simplification of the realistic system as
 179 it neglects, e.g., curvature and applies different boundary conditions (see
 180 Methods for details). However, it captures properly the long-range stress
 181 field of dislocations that was shown to play an essential role in the critical
 182 behaviour of dislocations^{3,23}. Since no length-scale other than the average
 183 dislocation spacing and the system size is present (due to the scale-free $1/r$ -
 184 type dislocation interactions) dimensionless variables denoted with $(\cdot)'$ are
 185 introduced hereafter (see Methods and Extended Data Table 1)^{24,25}.

186 A loading method analogous to the micropillar experiments is imple-
 187 mented, i.e., a platen is moved with velocity v'_p and the load is transferred
 188 to the system via a spring. As a result, dislocation avalanches appear as

189 stress drops here as well (Fig. 4b). During the avalanches, dislocations
190 move rapidly, and due to the overdamped dynamics assumed for dislocations
191 ($v' \propto F'$, where v' and F' is the velocity and the acting force for dislocations,
192 respectively) the elastic energy release rate reads as $\sum_i v_i'^2$, with the sum
193 performed over all dislocations. By thresholding this rate one can emulate
194 the sensitivity of the AE sensor and obtain simulated AE events as well as the
195 corresponding released energies (see Methods). Like in the experiments, the
196 simulated AE events show strong correlation with the stress drops (Fig. 4b,
197 Supplementary Videos 2, 3). It has been known that size distribution of dis-
198 location avalanches exhibits a different exponent in simulations compared to
199 the real samples^{23,26}, yet, the temporal clustering of the simulated AE events
200 shows very similar behaviour to experiments in terms of the correlation be-
201 tween stress jumps and the AE energies (Fig. 4c), Omori law (Fig. 4d), and
202 waiting time distribution (Fig. 4e). We thus conclude, that the complex dy-
203 namic behaviour observed in experiments is the result of the spatio-temporal
204 correlations of the dislocations due to their long-range elastic interactions
205 and the lack of short-range mechanisms, such as dislocation reactions.

206 **Outlook**

207 It has always been the fundamental assumption of AE experiments that the
208 parameters of the signals are characteristic of the local deformation process.
209 The experiments and simulations reported here prove this long-standing hy-
210 pothesis and reinforce that intermittency and scale-invariance characteriz-
211 ing plastic deformation of HCP single crystals (and, most likely, crystalline
212 metals/solids in general) are related to the self-organized critical (SOC) be-

213 haviour of dislocations. In addition, we showed that plastic events, simi-
214 larly to earthquakes, do not only exhibit spatial but also temporal clustering
215 with long-range correlations, however, the involved length and timescales are
216 profoundly different, as summarized in Extended Data Table 2. This phe-
217 nomenon also raises analogy with many other physical systems exhibiting
218 crackling noise²⁷. It is known, however, that SOC behaviour is not ubiq-
219 uitous in crystal plasticity, for instance, it is suppressed under multiple slip
220 conditions and at high temperatures^{28,29}. Dedicated further experiments and
221 modelling based on the new methodologies of this paper are needed to study
222 and understand whether dislocation dynamics is altered under such circum-
223 stances in terms of magnitude and spatiotemporal distribution of plastic
224 fluctuations.

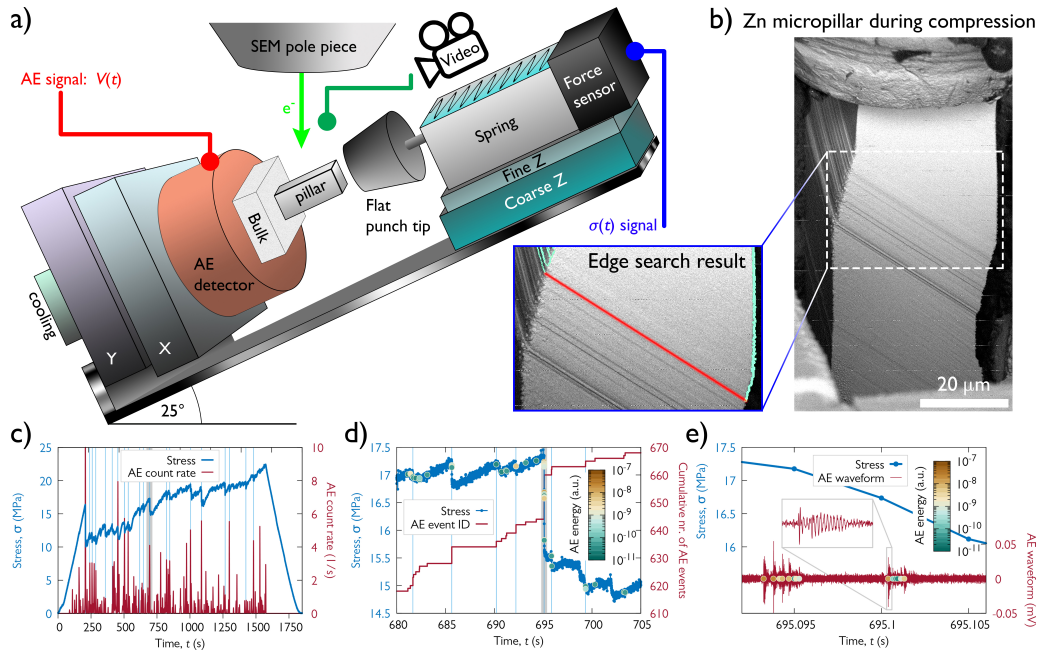


Figure 1: **Compression experiment of Zn micropillars oriented for single slip.** **a**, Sketch of the experimental set-up with a disproportionately large micropillar for clarity. **b**, Backscattered electron image of a $d = 32 \mu\text{m}$ micropillar during compression. The magnified image shows the slip band in red corresponding to the stress drop highlighted in grey in panels c and d. The location of the band was obtained by edge search on SEM images before and after the stress drop. **c**, Measured stress vs. time as well as the averaged rate (obtained by convolution with a Gaussian of 0.5 s width) of the detected individual AE bursts. The light blue vertical lines mark the stress drops larger than 1 MPa. **d**, Zoomed stress-time curve of the region shaded by grey in panel c. The coloured data points along the stress curve represent the individual AE events and their energies whereas the red curve shows the cumulative number of these events. The light blue vertical lines mark short periods with at least two AE events. **e**, Zoomed stress-time curve of the region shaded in grey in panel d and the detected AE waveform of the same interval. The inset shows the magnified view of a single event and coloured data points correspond to individual signals detected by thresholding the AE signal.

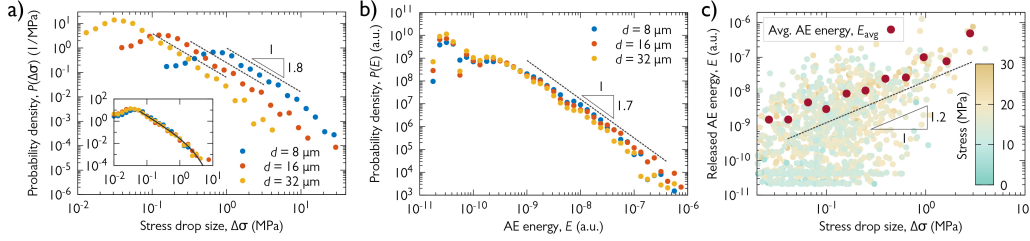


Figure 2: **Correlation between the stress drops and the acoustic signals.** **a**, Distribution of stress drop sizes $\Delta\sigma$ for different pillar diameters d . The probability density functions (PDFs) follow a power-law with exponent $\tau_\sigma = 1.8 \pm 0.1$. The inset shows the PDF as a function of the force drop $\Delta F = \Delta\sigma \cdot d^2$ with units in mN. The collapsed curves can be fit with a master function above the detection threshold and exhibit a cut-off at $F_0 = 1.5 \pm 0.1$ mN. **b**, Distribution of AE energies of individual signals detected at the sample surface. The curves are characterized by a power-law exponent $\tau_E = 1.7 \pm 0.1$ and do not exhibit an apparent cut-off and do not depend on the pillar diameter d . **c**, Scatter plot of the stress drops of $d = 32 \mu\text{m}$ pillars and the corresponding summed released AE energies. The color-scale refers to the actual stress at which the stress drop took place along the stress-time curve and do not show correlation with the size of the stress drop. The red dots represent the average released energies E_{avg} obtained by averaging the datapoints for stress drop size bins of logarithmically increasing width. The dashed line represents the $E \propto \Delta\sigma^\eta$ power-law relationship with the exponent found to be $\eta = 1.2 \pm 0.1$.

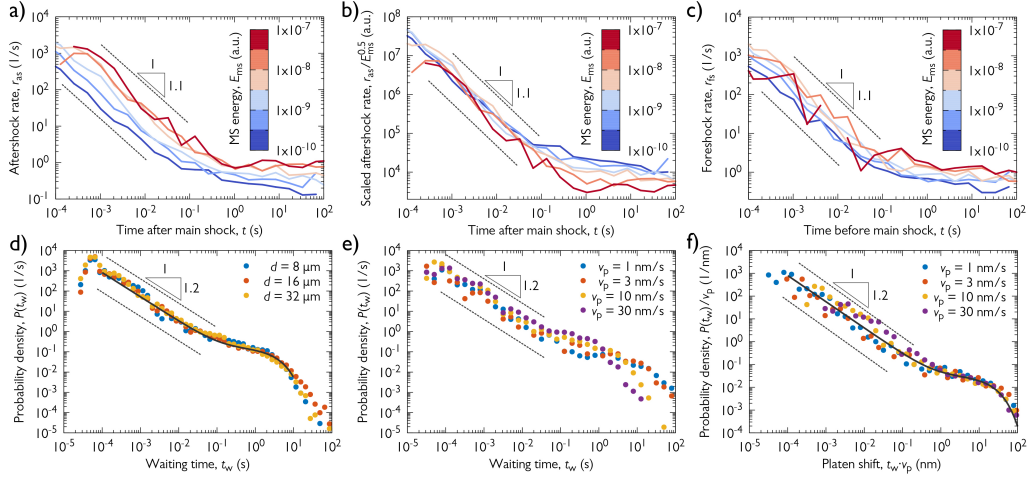


Figure 3: Temporal statistical analyses of AE events. **a**, The rate of aftershocks r_{as} after a main shock with an energy given by the colour for $d = 32 \mu\text{m}$ pillars (Omori law). **b**, Curves of panel a) divided with the square root of the main shock energy E_{ms} (aftershock productivity law). **c**, Rate of foreshocks r_{fs} before a main shock of energy given by the colours for $d = 32 \mu\text{m}$ pillars (inverse Omori law). **d**, PDF $P(t_w)$ of waiting times t_w between subsequent AE events for pillars of various sizes. **e**, $P(t_w)$ for $d = 8 \mu\text{m}$ pillars and different platen speeds v_p . **f**, $P(t_w)$ re-scaled with the platen velocity v_p . Note that the minimum t_w of $20 \mu\text{s}$, i.e., the minimum time between two subsequent AE events, is defined as one of the AE event individualization parameters (see Methods).

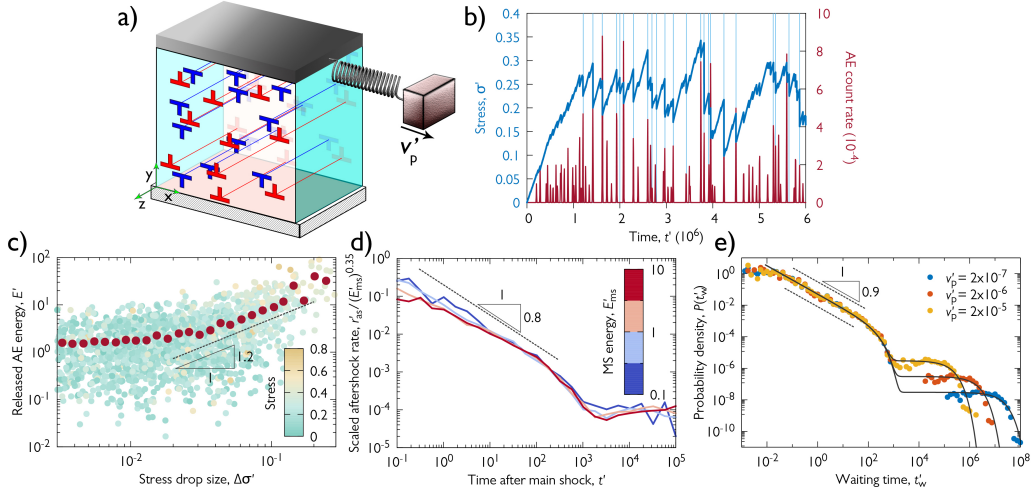


Figure 4: **DDD simulations.** **a**, Sketch of the simulation set-up. The system is infinite in direction z and periodic boundary conditions are applied in directions x and y . **b**, Stress vs. time curve as well as the averaged rate of the simulated individual AE bursts for a representative configuration. The light blue vertical lines show the stress drops larger than 0.02. **c**, Scatter plot of the stress drops and the corresponding summed released AE energies for systems of $N = 1024$ dislocations, see caption of Fig. 2c for details. **d**, The rate of aftershocks r'_{as} scaled with $(E'_{ms})^{0.35}$ after a main shock with energy E'_{ms} given by the colour for $N = 1024$ dislocations (Omori and productivity laws). **e**, PDF $P(t'_w)$ for $N = 256$ dislocations and different platen speeds v'_p .

225 **Methods**

226 **Sample preparation**

227 High purity single crystalline zinc heat treated at 100 °C for 4 h under at-
228 mospheric air, oriented for basal slip with side orientation corresponding to
229 the $\langle 2\bar{1}\bar{1}0 \rangle$ -type normal direction (Extended Data Fig. 2a) was mechanically
230 polished sequentially with SiC grinding paper and alumina suspension (down
231 to 1 μm). This was followed by a fast (10 s) electropolishing with Struers D2
232 solution at 20 V, 1 A. A sharp perpendicular edge was then created on the
233 bulk specimen by low energy Ar ion polishing (5 kV, 2 mA).

234 Experimental work including micropillar milling, EBSD measurements
235 and micromechanical testing was carried out inside the vacuum chamber of
236 an FEI Quanta 3D dual beam scanning electron microscope (SEM). Focused
237 ion beam (FIB) operating with Ga^+ ions was used to fabricate square-based
238 pillars of various sizes (8 μm : 13 pieces, 16 μm : 5 pieces and 32 μm : 4 pieces
239 with an approximate 3:1 aspect ratio of height to side), with final beam
240 conditions of 30 kV, 1 – 3 nA. In order to minimize Ga^+ ion contamination
241 on the surface and create practically non-tapered ($\leq 2.5^\circ$ between the side
242 and the loading axis) samples, the pillars were fabricated in a lathe milling
243 configuration³⁰. On the top of the pillars a thin (~ 350 nm) Pt cap was
244 deposited by FIB to act as hard buffer material between the pillars and the
245 flat punch tip and also to reduce ion contamination during FIB-milling.

246 Analytical methods

247 **Microstructure analysis**

248 For electron backscatter diffraction (EBSD) measurements, the Edax Hikari
249 camera was used with 1×1 binning, and the OIM Analysis v7 software pro-
250 vided the orientation results. Unit cell corresponding to the cross-sectional
251 side of the pillar can be seen in Extended Data Fig. 2. To calculate the
252 initial geometrically necessary dislocation (GND) density, a digital image
253 cross-correlation based technique called high (angular) resolution electron
254 backscatter diffraction (HR-EBSD) was applied³¹. The estimated average
255 value of $\rho^{\text{GND}} = 1.2 \times 10^{13} \text{ m}^{-2}$ was measured on a surface prepared by the
256 same FIB conditions as it was used for the pillar fabrication prior to de-
257 formation. This value is close to the detection limit of the GND density
258 by HR-EBSD, hence it is concluded that the sample preparation did not
259 introduce a significant/measurable dislocation content in the sample.

260 **X-ray line profile analysis**

261 Dislocation density characterization by X-ray diffraction measurements was
262 performed on the bulk Zn single crystal sample prior to the micropillar
263 fabrication. The X-ray line profiles of the $(10\bar{1}1)$ reflection were obtained
264 by a double-crystal diffractometer using Cu $K\alpha$ radiation (Extended Data
265 Fig. 5a). The experimental setup is of $\theta - 2\theta$ type, that consists of a high
266 intensity Rigaku RU-H3R rotating anode X-ray generator with a copper an-
267 ode, a monochromator that filters out the Cu $K\alpha_2$ component and redirects
268 the X-ray beam to the sample, and the Dectris MYTHEN 1D wide range
269 solid state X-ray detector that records the peak at a distance of 960 mm. We

270 also used a cylindrical vacuum chamber between the sample and the detec-
 271 tor in order to increase the peak-to-background ratio. The quantification of
 272 the total dislocation density was carried out by the variance method^{32,33} by
 273 analyzing peak broadening based on the asymptotic behaviour of the second
 274 order restricted moment:

$$M_2(q) = \frac{1}{\pi^2 \epsilon_F} q + \frac{\Lambda}{2\pi^2} \langle \rho \rangle \ln \frac{q}{q_0}, \quad (1)$$

275 where $q = 2(\sin \theta - \sin \theta_0)/\lambda$, λ corresponds to the wave length of the applied
 276 X-rays, and θ and θ_0 are half of the diffraction and Bragg angles, respectively.
 277 Parameter q corresponds to the distance from the peak center in reciprocal
 278 space, q_0 is a constant depending on the dislocation-dislocation correlations,
 279 ϵ_F is the coherent domain size, and $\langle \rho \rangle$ is the average dislocation density.
 280 The value of Λ is commonly given as $\Lambda = 2|\mathbf{g}|^2|\mathbf{b}^2|C_g/\pi$, where \mathbf{b} and \mathbf{g} are
 281 the Burgers and diffraction vectors, respectively, and C_g is the diffraction
 282 contrast factor that depends on the type of dislocations in the system and
 283 on the relative geometrical position between the dislocation line direction \mathbf{l}
 284 and the direction of \mathbf{g} .

285 As the coherent domain size is larger than $\sim 1 \mu\text{m}$, the first term in Eq. (1)
 286 is negligible. As a result of the second term caused by the dislocations, M_2
 287 versus $\ln(q)$ plot indeed becomes a straight line in the $q \rightarrow \infty$ asymptotic
 288 regime, as shown in Extended Data Fig. 5b. From the fit a total dislocation
 289 density of $\langle \rho \rangle^{\text{XRD}} = (7.5 \pm 0.5) \times 10^{13} \text{ m}^{-2}$ was obtained. As expected,
 290 this value is higher than the GND density determined by the HR-EBSD
 291 technique, therefore it can be assumed that the initial dislocation network
 292 mostly consisted of statistically stored dislocations.

293 Micromechanical experiments

294 **Testing device**

295 Room temperature compression tests on the micropillars were carried out
296 in high vacuum mode inside the SEM chamber to allow *in situ* monitor-
297 ing of the deformation process and slip activity on the pillars' surface by
298 secondary and backscattered electrons. A custom-made nanoindenter^{34,35}
299 shown in Extended Data Fig. 1 was used without any load or strain feed-
300 back loop integrated. The precision of the indentation depth and load was
301 ~ 1 nm and ~ 1 μ N, respectively. The applied sampling rate was 200 Hz, while
302 platen velocity (if not stated otherwise) and spring constant were 10 nm/s
303 and 10 mN/ μ m, respectively. For a detailed description of the device, the
304 reader is referred to³⁴. Exemplary stress-strain curves are presented in Ex-
305 tended Data Fig. 6. The curves show the intermittent nature of plasticity in
306 micropillars and also provide evidence of the so-called plasticity size effect
307 ('smaller is harder').

308 **Edge detection**

309 In order to investigate the spatial distribution of the plastic strain corre-
310 sponding to individual stress drops, edge detection was performed sequen-
311 tially on each SEM image of the $d = 32$ μ m micropillar shown in Fig. 1b.
312 We aimed at detecting the vertical edge on the right side of the micropillar
313 as it was characterized by a large difference in the intensity in the horizontal
314 direction (due to the dark background). First, a vertical line was selected
315 at the middle of the pillar as a reference. To detect the sudden change in
316 intensity the pictures were then processed row by row starting from the ref-

317 erence line. If the drop in the intensity was larger than the given threshold,
318 the point was marked as part of the edge. The raw images were processed
319 using the OpenCV package³⁶.

320 The used backscattered electron detector introduced high intensity noise
321 in the form of short horizontal lines with a width of few pixels, which needed
322 to be filtered. Noise filtering was applied with the Savitzky-Golay filter of
323 the SciPy library³⁷ with window size selected to be 11 pixels and the order
324 of the fitted polynomial selected to be 2.

325 The time development of the edge is shown in Extended Data Fig. 7.
326 The base of the sample was moved to the origin and the results were rotated
327 by one degree clockwise. The white gaps represent strain bursts when large
328 plastic deformation occurs between consecutive images. The slip band can
329 be located by determining the end of the gap. As seen, the gaps end at
330 well-defined points, confirming that strain bursts take place within ‘thin’ slip
331 bands.

332 Based on Extended Data Fig. 7, the SEM images recorded before and
333 after the stress drop analysed in Figs. 1c-e were identified and the corre-
334 sponding edge shapes were denoted by purple and pink colours, respectively.
335 These SEM images are shown in Extended Data Figs. 8a-b. Although it is
336 barely seen by visual inspection, the quantified difference of the two images
337 (Extended Data Figs. 8c) proves that deformation took place along the slip
338 plane at the height of $\sim 28 \mu\text{m}$ (as also seen as horizontal grey line in Ex-
339 tended Data Fig. 7 and highlighted by a red line along the corresponding
340 basal plane in Fig. 1b).

341 AE measurements

342 **Detecting AE signals**

343 By definition, acoustic emissions are transient elastic waves generated in ma-
344 terials due to sudden localized and irreversible structure changes³⁸. The
345 detection of AE waves is based on its physical nature – when the material
346 is subjected to external loading, released energy forms stress pulses propa-
347 gating through the material as transient elastic waves. The wave component
348 perpendicular to the surface is detected typically by a piezoelectric trans-
349 ducer (attached directly to the specimen surface), which converts recorded
350 displacements into an electrical signal.

351 The nanoindenter device was equipped with a Physical Acoustics Corpo-
352 ration (PAC) WS α wide-band (100-1000 kHz) AE sensor, which showed a
353 superior combination of frequency and sensitivity characteristics over other
354 tested sensors (PAC Micro30S, PAC F15I-AST). The Zn single-crystal (with
355 FIB-milled micropillars on the surface) was attached to the transducer over
356 a layer of vacuum grease to ensure effective acoustic coupling. Mechanical
357 bonding ('clipping') was carried out by means of a thin metallic strip bent
358 over the sample and fixed at both ends to the device, ensuring a constant
359 contact pressure during the compression tests. The recorded signal was am-
360 plified using the Vallen AEP5 pre-amplifier set to 40 dB_{AE}. Data acquisition
361 and processing were performed using the computer-controlled Vallen AMSY-
362 6 system. Data acquisition was carried out in continuous data streaming
363 mode, i.e., the whole raw acoustic data sets were recorded for further post-
364 processing at a sampling rate of 2.5 MHz.

365 **Identification of AE events**

366 To individualize the AE events, an in-house script implemented in Matlab
367 was used. The threshold voltage was set to $V_{\text{th}} = 0.01$ mV, this value being
368 slightly above the background noise. The hit definition time (HDT), i.e., the
369 minimum period between two subsequent AE events, used for the separation
370 of events was $20 \mu\text{s}$.

371 In Extended Data Fig. 9 various parameters of a representative event
372 related to the AE measurements are defined. The original AE waveform
373 $V(t)$ is plotted in the inset as a function of time t . The AE event energy is
374 defined as the area under the squared signal amplitude curve:

$$E = \int_{t_b}^{t_e} V^2(t) dt, \quad (2)$$

375 where t_b and t_e denote the beginning and end of the event, respectively (that
376 is, E is the extent of the area shaded in blue in Extended Data Fig. 9).
377 The AE counts are defined as the number of data points (in absolute values)
378 crossing the threshold level V_{th} . The duration of one AE event is defined as
379 the time between the first and the last AE count in that event.

380 **Data validation**

381 The common source of both load drops and AE events in the tested mi-
382 cropillars are dislocation avalanches in the basal plane. In order to exclude
383 any other external effects that might lead to the generation of AE events,
384 additional aspects of the AE measurement had to be addressed: (i) friction
385 between the indenter's flat diamond tip and the top of the pillars and (ii)
386 possible noise or vibrations from external sources and the nanotesting device
387 itself.

388 To address point (i) we investigated six micropillars with identical geom-
 389 etry, fabricated by three different methods for this purpose. Two pillars were
 390 prepared with Pt coating, two with C coating and two pillars without any
 391 coating on top. Although three materials with different friction properties
 392 were used, the analysis produced practically identical results with respect
 393 to the AE events and strain bursts. To avoid the presence of any spurious
 394 extrinsic vibrations considered within point (ii), three further compression
 395 tests were carried out where a special tip suspension was applied – another
 396 elastic part (a piece of rubber) was added to the device to isolate possible
 397 vibrations and noises from external sources. Just as in the previous case (i),
 398 this analysis demonstrated that there were no observable differences in the
 399 AE data compared to the tests without this additional suspension.

400 **The overlapping of AE events**

401 Assuming that the AE events originate from individual well-defined plastic
 402 events (i.e., dislocation avalanches related to stress drops) and there are no
 403 significant scattering and echoing mechanisms during the wave propagation,
 404 one may expect an exponential decay of the waveform resulting from intrinsic
 405 absorption^{39,40}. In that case, the relationship between the maximum squared
 406 amplitude

$$A^2 = \max_{t \in [t_b, t_e]} V^2(t), \quad (3)$$

407 and the duration $T = t_e - t_b$ could be written as

$$A^2(T) = V_{th}^2 \exp\left(\frac{T}{\tau}\right), \quad (4)$$

408 where τ is a timescale characterizing the rate of absorption⁴⁰. This rela-
 409 tion was fitted to all data points that were detected under the same noise

410 conditions. This set of data contained more than 13,000 events from the
 411 compression tests on Zn pillars with various dimension. The data trends and
 412 exponential fits shown in Extended Data Fig. 10 prove the validity of relation
 413 (4); thus, we concluded that the majority of detected events are due to short
 414 pulse-like events at the source attenuated only by intrinsic absorption, while
 415 recording of wave reflections and overlapping events is not common with the
 416 AE event individualization parameters used in this study (see above). It is
 417 also noted, that the fitted value of $\tau = 45 \mu\text{s}$ is below the typical time-scales
 418 characteristic of the Omori-law and waiting time distributions in Fig. 3.

419 **Rates of aftershocks and foreshocks**

420 Large AE events, similarly to earthquakes, are usually followed by several
 421 aftershocks. To quantify the rate of these aftershocks the following procedure
 422 was implemented. First, we select an energy interval $[E_{\text{ms}} - \Delta E/2, E_{\text{ms}} +$
 423 $\Delta E/2]$ and consider only AE events with energies falling in this given bin.
 424 These will be the main shocks with energy E_{ms} . The sequence of events
 425 (aftershocks) corresponding to each main shock lasts until an event with
 426 energy falling in this or larger bin takes place. The time after the main shock
 427 t is binned logarithmically, and the AE events in the sequence following the
 428 main shock falling in each bin are counted, and then repeated for all main
 429 shocks with energy E_{ms} . To obtain the rate of the aftershocks $r_{\text{as}}(t)$ the
 430 number of events in the time bin around t is normalized with the bin width
 431 and also with the number of sequences that reached the given length t . The
 432 obtained $r_{\text{as}}(t)$ curves for $d = 32 \mu\text{m}$ pillars are plotted in Figs. 3a-b. The
 433 corresponding figures for smaller micropillars are shown in Extended Data
 434 Figs. 4a-d.

435 In the case of foreshock rates r_{fs} the same procedure was adopted and
436 inverted in time to investigate sequences before main shocks. The obtained
437 rates for $d = 32 \mu\text{m}$ pillars are seen in Fig. 3c and for smaller ones in Extended
438 Data Figs. 4e-f.

439 **Waiting time of AE events**

440 The waiting time distributions of Figs. 3d-f are obtained as follows. The
441 identification of the individual AE events described above in section ‘Identi-
442 fication of AE events’ yields the time t_i of each event. The waiting time is
443 then simply $t_{w,i} = t_{i+1} - t_i$, and the distribution of these values is computed.

444 Since only those AE events can be detected that rise above the back-
445 ground noise, it is important to check the role of thresholding in the obtained
446 distributions. To this end, the procedure described above was repeated after
447 considering only events with energies E larger than a threshold E_{th} . Ac-
448 cording to Extended Data Fig. 11a they only differ in the exponential tail
449 characterized by parameter t_0 related to the average time between subse-
450 quent uncorrelated event clusters. As seen, increase of E_{th} leads to fewer
451 detected events and, thus, an increased t_0 . To prove that thresholding does
452 not influence the conclusions of the paper, in Extended Data Fig. 11b the
453 distributions were re-scaled with the average waiting time $\langle t_w \rangle$ correspond-
454 ing to the given threshold E_{th} . The obtained collapse of the curves means
455 that $t_0 \propto \langle t_w \rangle$ similarly to what was obtained in the case of different platen
456 velocities v_p (Figs. 3e-f), and it proves scale-invariance of the AE events.

457 Simulations

458 **Discrete dislocation dynamics**

459 The model to be investigated is one of the simplest discrete dislocation sys-
460 tems that still incorporates the following fundamental physical properties of
461 dislocations:

- 462 • $1/r$ -type long-range interactions between dislocation lines.
- 463 • Non-conservative motion of dislocations due to the strong phonon drag.
- 464 • Geometrically constrained motion of dislocation lines, since at low tem-
465 peratures they can only glide in certain planes (called glide planes).
466 As a result, the system cannot reach a global energy minimum state,
467 rather, it gets trapped in a meta-stable configuration.

468 The system consists of straight edge dislocations parallel with the z axis,
469 and their slip planes are parallel with the xz plane (single slip). Since the
470 system is translationally invariant along the z axis it can be considered two-
471 dimensional (2D) and it is sufficient to track the motion of dislocations in the
472 xy plane. In this set-up the Burgers vector points in the x direction and, thus,
473 reads as $\mathbf{b} = s(b, 0)$, where $s \in \{+1, -1\}$ is the *sign* of the dislocation, that
474 can be understood as some kind of charge. Extended Data Fig. 12a shows an
475 example of such a 2D dislocation configuration. The colours of dislocations
476 represent their sign and the background colour refers to the local shear stress
477 within the embedding elastic medium.

478 Because of the strong dissipation due to phonon drag, the motion of
479 dislocations is assumed to be overdamped, that is, the force acting on a

480 dislocation of unit length is proportional to its velocity. If the system consists
 481 of N dislocations and $\mathbf{r}_i = (x_i, y_i)$ denotes the position of the i th ($i =$
 482 $1, \dots, N$) dislocation then the equation of motion reads as

$$\dot{x}_i = Ms_i b \left[\sum_{j=1; j \neq i}^N s_j \sigma_{\text{ind}}(\mathbf{r}_i - \mathbf{r}_j) + \sigma \right], \quad (5)$$

$$\dot{y}_i = 0. \quad (6)$$

483 Here M is the dislocation mobility, σ is the externally applied shear stress
 484 and σ_{ind} is the shear stress field generated by individual dislocations. For the
 485 latter the solution corresponding to isotropic continua is used⁴¹:

$$\sigma_{\text{ind}}(\mathbf{r}) = \frac{\mu b}{2\pi(1-\nu)} \frac{x(x^2 - y^2)}{(x^2 + y^2)^2}, \quad (7)$$

486 where μ and ν denotes the shear modulus and the Poisson number, respec-
 487 tively. Dislocations are arranged in a square-shaped simulation area and
 488 periodic boundary conditions (PBC) are applied. The emerging image dis-
 489 locations alter the stress field of Eq. (7) (that corresponds to an infinite
 490 medium), which can be obtained using a Fourier method (see Extended
 491 Data Fig. 12b)⁴². The equations of motion (5,6) are solved using a fully
 492 implicit scheme that makes usage of annihilation unnecessary, so, it is not
 493 implemented⁴³.

494 One of the main advantages of the model system introduced is that the
 495 dislocation interactions exhibit a $1/r$ -type decay. This means that apart from
 496 the average dislocation spacing (being equal to $\rho^{-0.5}$, where ρ is the total dis-
 497 location density) no additional length scales appear in the model. One may,
 498 thus, introduce dimensionless variables by measuring length, stress, strain
 499 and time in units summarized in Extended Data Table 1, where notation
 500 $G = \mu/[2\pi(1-\nu)]$ is introduced.

501 Initially, an equal number of positive and negative sign dislocations are
502 positioned randomly in the square-shaped simulation area with uniform dis-
503 tribution. At zero applied stress the system is first let to evolve into a relaxed
504 equilibrium configuration. After that the applied shear stress is increased us-
505 ing a protocol emulating the experimental set-up of micropillar compression.
506 Namely, the applied stress is computed at every time step according to

$$\sigma' = r'(v_p' t' - \varepsilon' L'), \quad (8)$$

507 where v_p' is the platen velocity (see Fig. 4a), t' is the simulation time, r' is
508 a constant characterizing the strength of the spring connecting the platen
509 and the dislocation system, and ε' is the accumulated plastic shear strain
510 computed as:

$$\varepsilon'(t') = \sum_{i=1}^N s_i [x_i'(t') - x_i'(0)]. \quad (9)$$

511 In the simulations $r' = 1/32$ was used and the platen velocity (if not stated
512 otherwise) was set to $v_p' = 1.6 \times 10^{-4}$.

513 **Event detection**

514 The overdamped dynamics used in Eqs. (5,6) reflects the fact that dislocation
515 motion is a highly dissipative process during which stored elastic energy E'_{el}
516 of the embedding crystal is transformed into other types of energies (e.g., heat
517 or elastic waves). This energy dissipation rate r'_{en} can be obtained as

$$r'_{en} = -\dot{E}'_{el} = \sum_{i=1}^N (v_i')^2, \quad (10)$$

518 where $v_i' = \dot{x}_i'$ is the velocity of the i th dislocation.

519 Stress drop detection is based on the finding that in active periods the
520 dissipation rate r'_{en} increases several orders of magnitudes as demonstrated
521 on an exemplary event in Extended Data Fig. 13. To obtain the beginning
522 t'_b and end t'_e of the event a threshold of $r'_{\text{th}} = 5 \cdot 10^{-6}$ was used for the
523 dissipation rate as demonstrated in Extended Data Fig. 13. The size of the
524 stress drop then follows as $\Delta\sigma' = \sigma'(t'_e) - \sigma'(t'_b)$.

525 As seen in Extended Data Fig. 13, a plastic event exhibits a fine struc-
526 ture with many peaks in the dissipation rate r'_{en} . In order to emulate an
527 AE detector, an additional threshold $r'_{\text{th,AE}}$ is defined that characterises the
528 sensitivity of the detector: whenever $r'_{\text{en}} > r'_{\text{th,AE}}$ the detector is able to mea-
529 sure the dissipation rate. With this, emulated AE events can be defined as
530 demonstrated in the inset of Extended Data Fig. 13. The threshold $r'_{\text{th,AE}}$
531 breaks up the signal in individual AE events, with their energy E' being the
532 size of the area shaded alternately in blue and red colour. Data processing
533 was carried out with the utilization of the NumPy library⁴⁴.

534 From the list of stress drops and AE events the AE count rate, the cor-
535 relation between stress drops and AE energies, the aftershock rates and the
536 waiting time distributions in Figs. 4b-e were determined with the same pro-
537 cedure as for experiments. The role of the threshold $r'_{\text{th,AE}}$ used to model
538 AE detector sensitivity was also investigated. According to Extended Data
539 Fig. 14 the Omori law as well as the productivity law are recovered in a
540 wide range of thresholds, however, small thresholds lead to the coalescence
541 of events leading to a deviation from the power-law behaviour for small times
542 t' . In Figs. 4d-e $r'_{\text{th,AE}} = 3.16$ was used for AE individualization.

543 **Data availability**

544 All data are available in the main Article and Methods, or from the corre-
545 sponding author upon reasonable request.

546 **Code availability**

547 The numerical methodology used in this study is described in Methods and
548 the source code is available at:

549 <https://github.com/pgabor/dislocation-avalanches-earthquakes>.

550 **Acknowledgements**

551 The work was performed within the ELTE Institutional Excellence Program
552 (TKP2020-IKA-05) supported by the Hungarian Ministry of Human Capac-
553 ities. P.D.I, D.U., G.P., D.T. and I.G. acknowledge support by the National
554 Research, Development and Innovation Fund of Hungary (contract number:
555 NKFIH-K-119561). This research received financial support from the Czech
556 Science Foundation, Grant No. 19-22604S (M.K. and F.C.).

557 **Author Contributions**

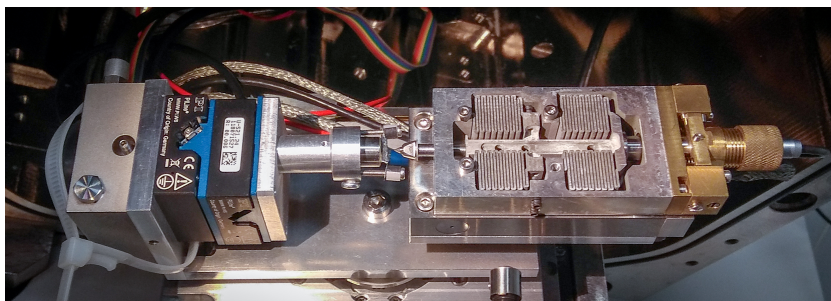
558 P.D.I. designed the research and supervised the project. P.D.I., D.U., Z.D.,
559 D.T. and I.G. designed and developed the microdeformation stage. D.U. per-
560 formed micropillar fabrication and compression experiments as well as EBSD
561 and X-ray measurements. D.U., M.K., K.M. and F.C. performed the AE
562 measurements. S.K. assisted with the sample preparation and analysis.
563 P.D.I., D.U. and S.K. analysed the experimental data. I.G. assisted at every

564 experimental measurement. G.P. developed and performed the simulations
565 and performed the slip band analysis. P.D.I., D.U., G.P., S.K., M.K. and
566 K.M. wrote the paper, with contributions from all authors.

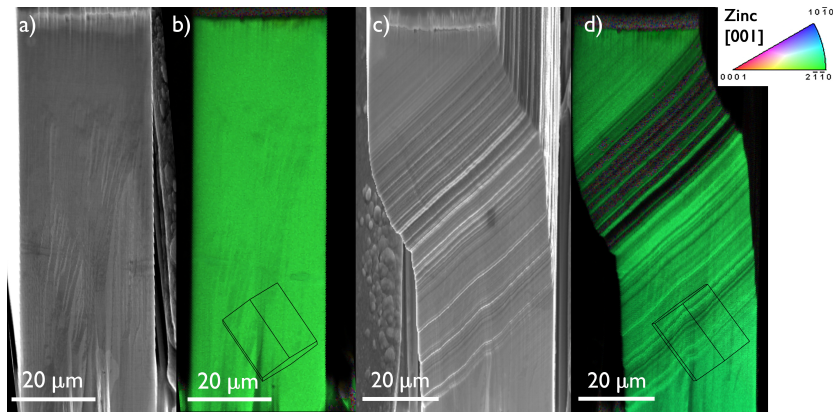
567 **Competing Interests Statement**

568 The authors declare no competing interests.

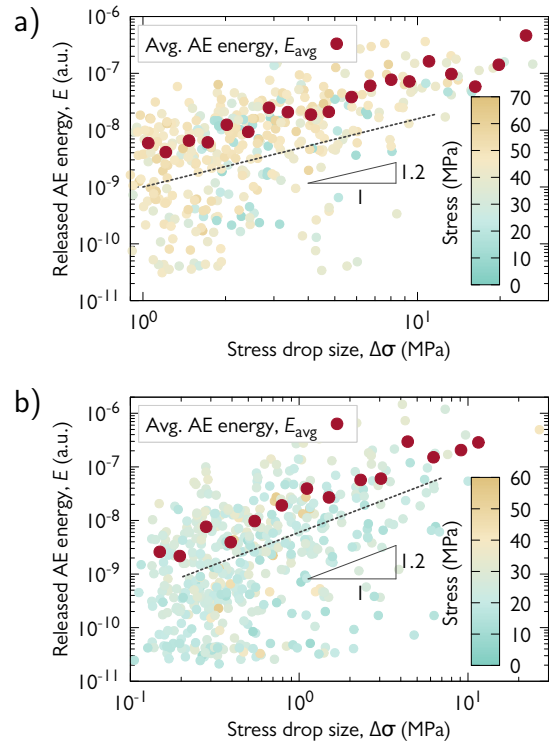
569 Extended data figures and tables



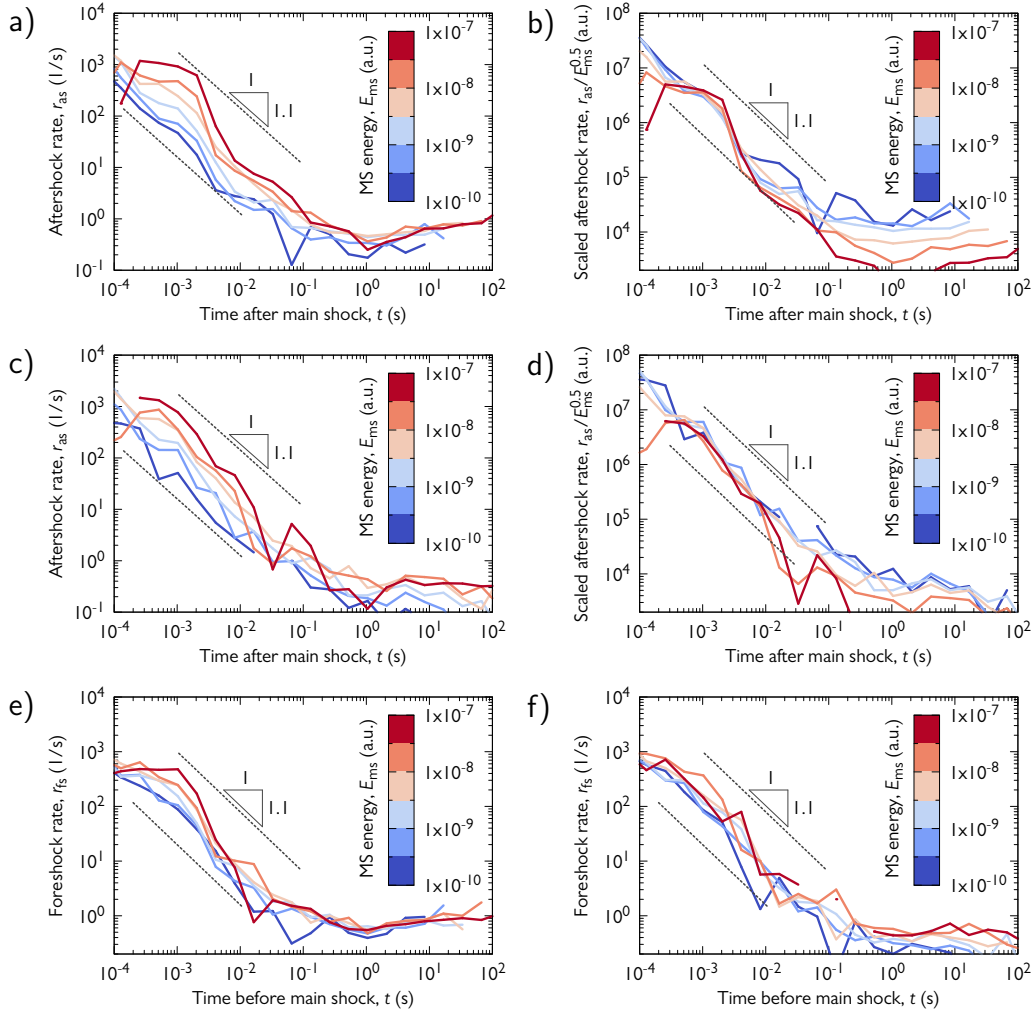
Extended Data Figure 1: In-house developed *in situ* nanoindentation set-up.



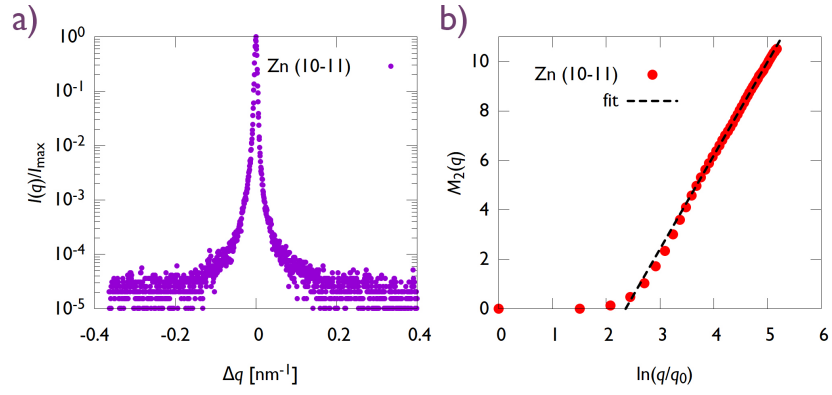
Extended Data Figure 2: **SEM imaging of the micropillars.** **a, c,** Secondary electron image of the same pillar in a tilt-corrected (70°) view before and after deformation. Note the uni-directional parallel slip bands in the deformed pillar. **b, d,** EBSD orientation map measured before and after compression of a Zn micropillar. The uniform color confirms single crystal structure both before and after the deformation. The orientation of the unit cell is also shown proving that the slip bands are parallel with the basal plane of the crystal.



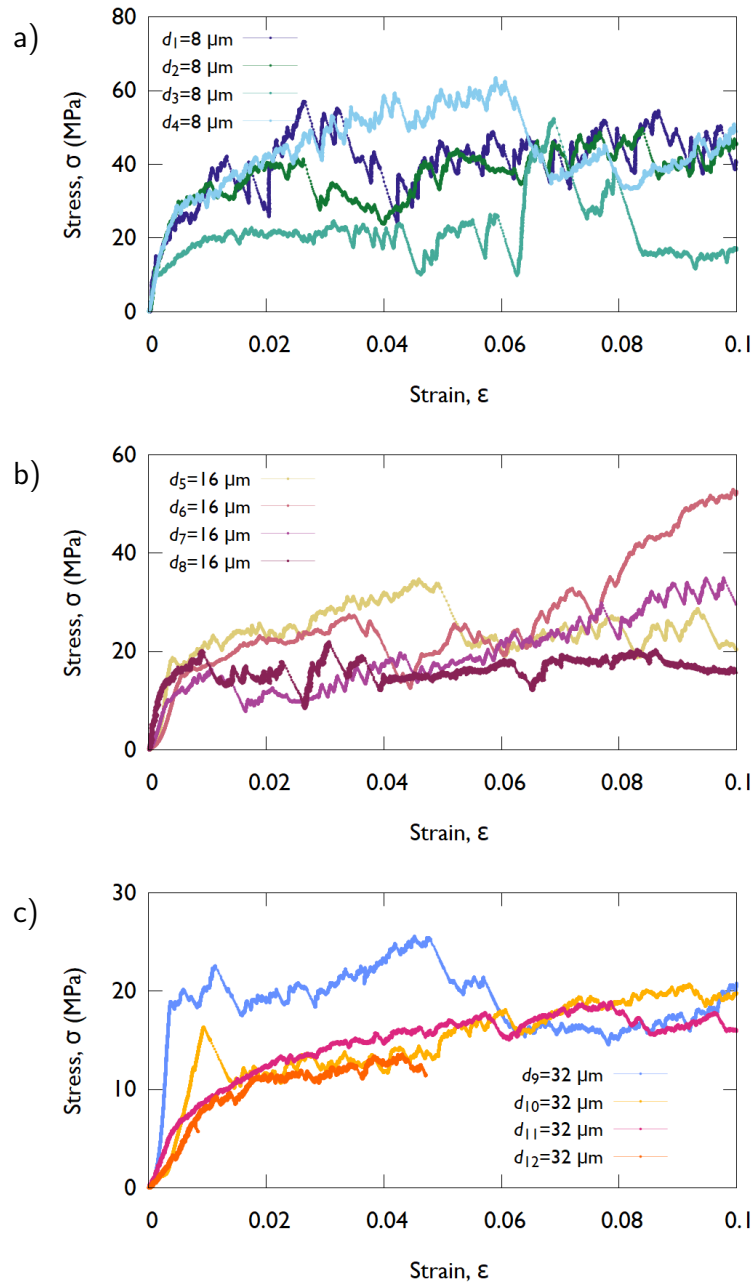
Extended Data Figure 3: **Correlation between stress drops and released AE energy.** **a**, Equivalent figure to that of Fig. 2c for $d = 8 \mu\text{m}$ micropillars. **b**, Equivalent figure to that of Fig. 2c for $d = 16 \mu\text{m}$ micropillars.



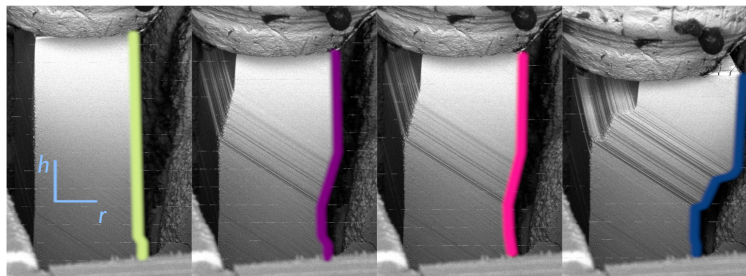
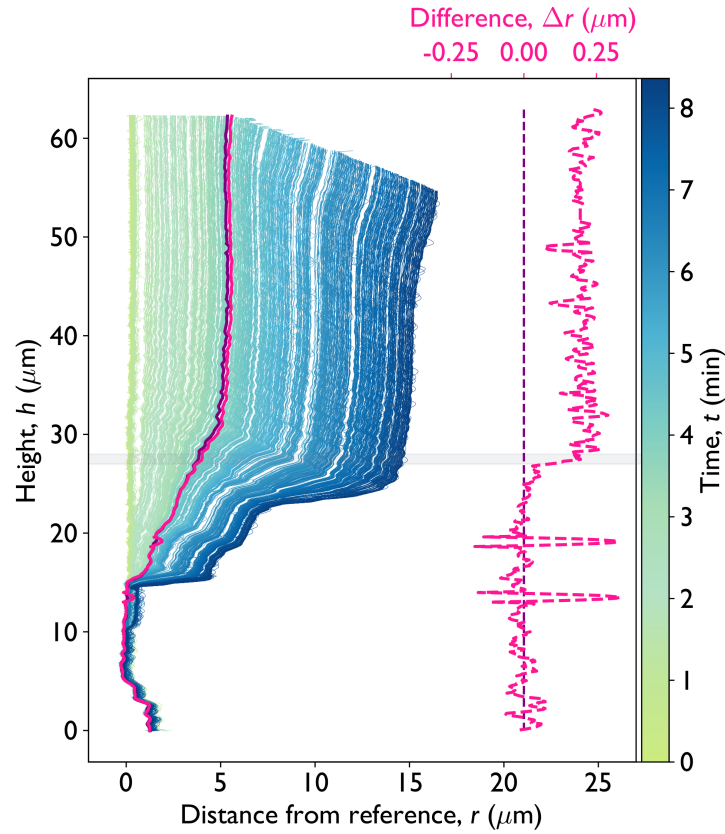
Extended Data Figure 4: **Aftershock and foreshock rates for $d = 8 \mu\text{m}$ and $d = 16 \mu\text{m}$ micropillars.** **a**, Aftershock rates r_{as} after main shocks of various energies E_{ms} for $d = 8 \mu\text{m}$ micropillars. **b**, Aftershock rates r_{as} of panel a) scaled with $E_{ms}^{0.5}$ for $d = 8 \mu\text{m}$ micropillars. **c**, Aftershock rates r_{as} after main shocks of various energies E_{ms} for $d = 16 \mu\text{m}$ micropillars. **d**, Aftershock rates r_{as} of panel a) scaled with $E_{ms}^{0.5}$ for $d = 16 \mu\text{m}$ micropillars. **e**, Foreshock rates r_{fs} before main shocks of various energies E_{ms} for $d = 8 \mu\text{m}$ micropillars. **f**, Foreshock rates r_{fs} before main shocks of various energies E_{ms} for $d = 16 \mu\text{m}$ micropillars.



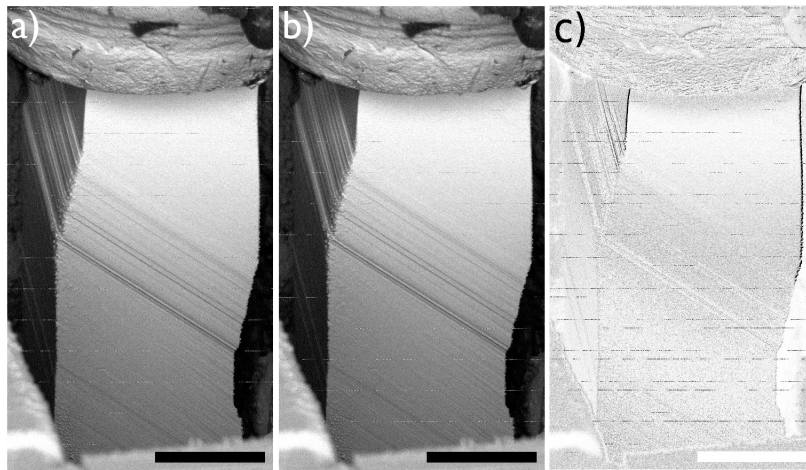
Extended Data Figure 5: **X-ray diffraction measurements on the original bulk Zn sample.** **a**, The measured X-ray line profile of the $(10\bar{1}1)$ reflection of the Zn single crystal. **b**, Second restricted moment M_2 as a function of $\ln q/q_0$, with $q_0 = 1 \text{ nm}^{-1}$. Dislocation density can be obtained from the linear fit from Eq. (1).



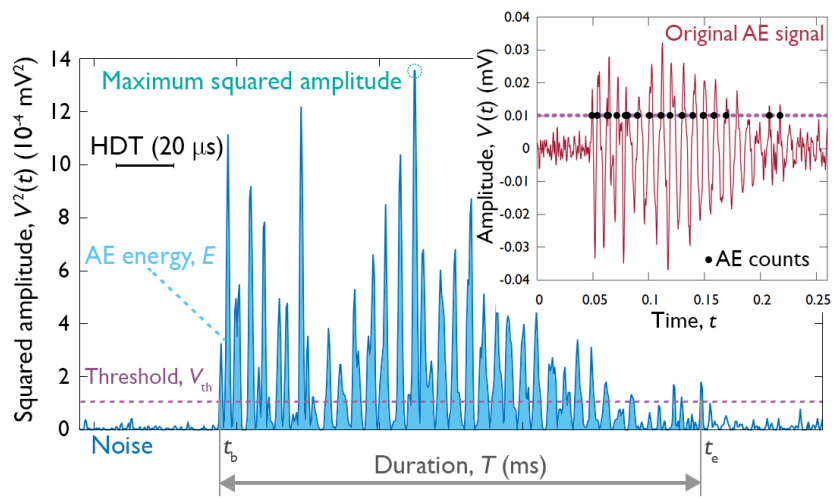
Extended Data Figure 6: **Exemplary stress-strain curves of micropillars of various sizes.** **a**, $d = 8 \mu\text{m}$, **b**, $d = 16 \mu\text{m}$ and **c**, $d = 32 \mu\text{m}$ pillars.



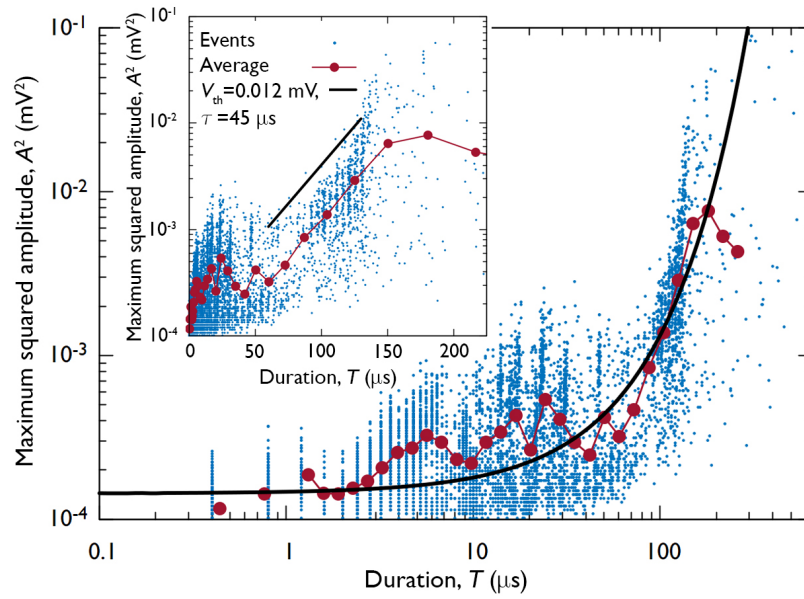
Extended Data Figure 7: **Time development of the right edge of the micropillar.** Distance from the reference line with the corresponding height as a function of time indicated by the colour for the micropillar shown in Fig. 1b. The purple and pink lines indicate the pillar shape before and after the stress drop investigated in Figs. 1c-e, respectively. The light gray horizontal line highlights the place where slip occurred.



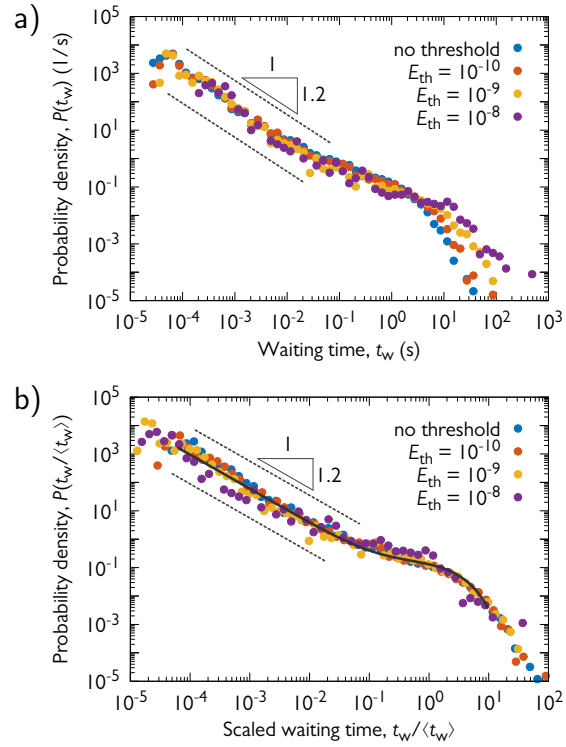
Extended Data Figure 8: **Locating spatial distribution of a strain burst.** **a, b,** Backscattered electron images of the micropillar before and after the stress drop analysed in Figs. 1c-e. The scale bar represents 20 μm . **c,** The difference of panels a) and b). The dark edges at the upper part of the pillar are due to plastic slip that occurred on the slip band highlighted in red in Fig. 1b.



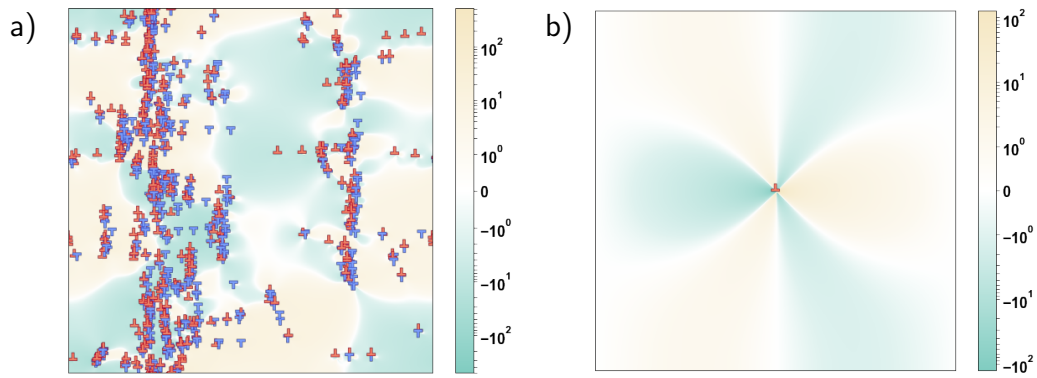
Extended Data Figure 9: **Parameters of a typical AE event.** Squared amplitude $V^2(t)$ of the AE signal as a function of time, showing the definitions of the AE parameters. The energy is the area of the region shaded in light blue. The inset presents the original waveform.



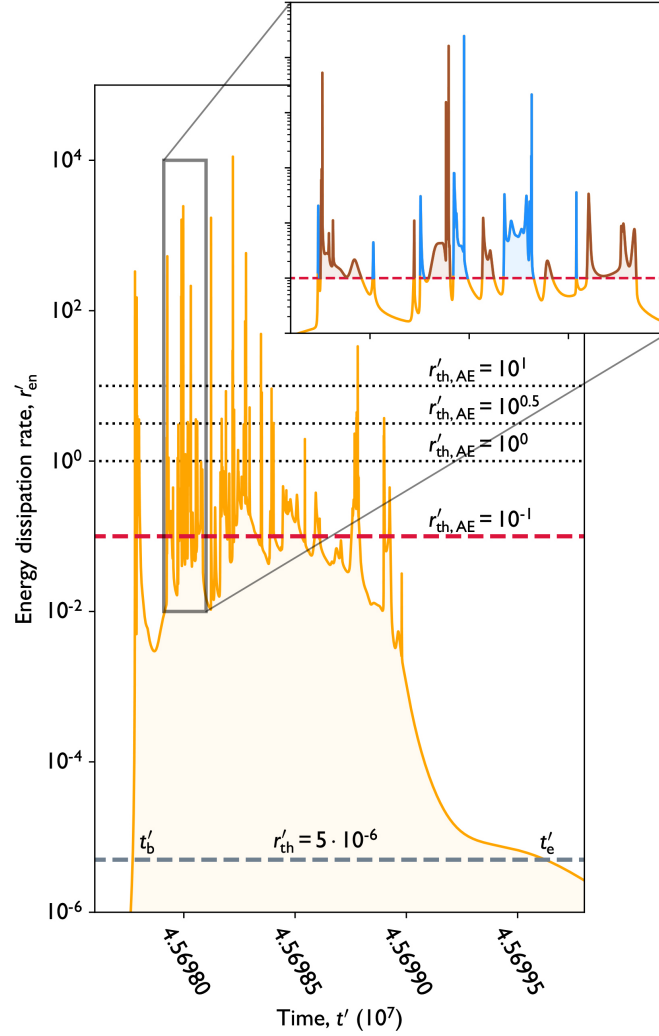
Extended Data Figure 10: **Analysis of AE signal attenuation.** Scatter plot of the maximum squared amplitude of individual AE events and their duration. The red data points represent the average relationship obtained by logarithmic binning with respect to the signal duration. Black solid line corresponds to the fit according to Eq. (4).



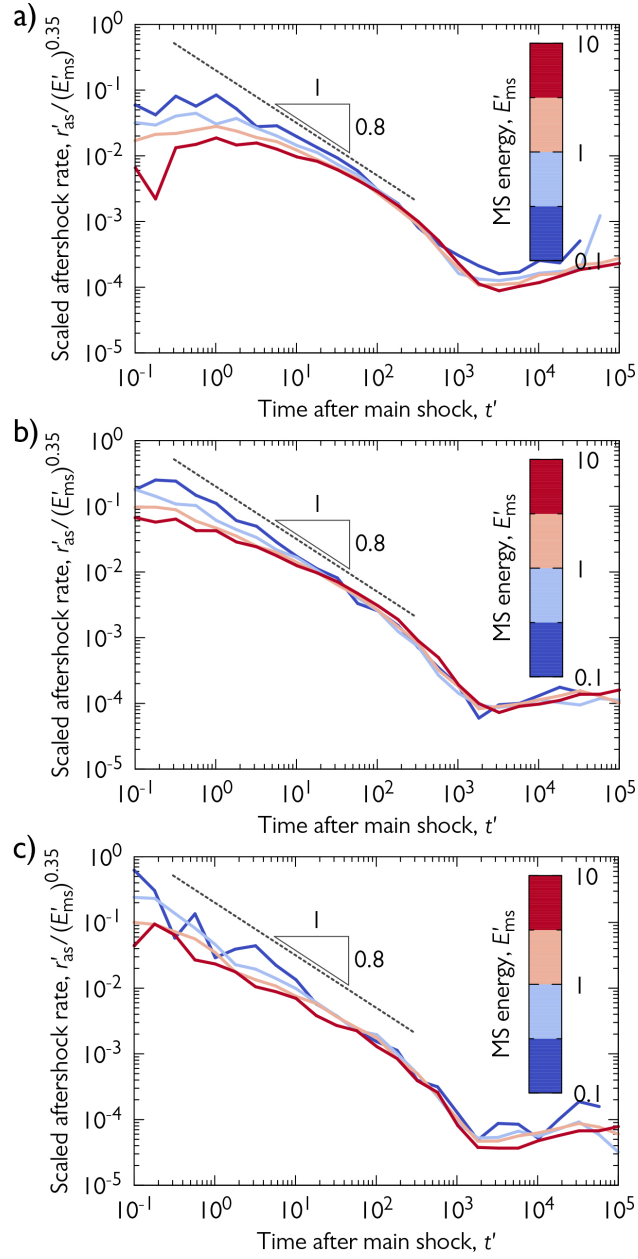
Extended Data Figure 11: **Effect of thresholding on waiting time distributions of $d = 32 \mu\text{m}$ micropillars.** **a**, Waiting time distributions for AE events with energies larger than E_{th} . **b**, Distributions of panel a) re-scaled with the average waiting time of the events. The master curve fitting the collapsed curves is identical to that of Fig. 3f.



Extended Data Figure 12: **2D discrete dislocation dynamics simulations.** **a**, An exemplary configuration with 512 positive (red) and 512 negative (blue) sign dislocations. The background colour and the colour scale refers to the internal shear stress generated by the individual dislocations. **b**, Shear stress field of an individual positive sign dislocation σ'_{ind} with periodic boundary conditions applied at all edges of the square-shaped simulation area.



Extended Data Figure 13: **Event individualization in DDD simulations.** The time dependence of the energy dissipation rate r'_{en} during an exemplary plastic event (also shown in Supplementary Video 3). The thick horizontal black line denotes the threshold r'_{th} used for identification of a plastic event, whereas dotted horizontal black lines refer to thresholds $r'_{th,AE}$ used to individualize emulated AE bursts. The inset shows the identified AE bursts that took place during the stress drop at $r'_{th,AE} = 0.1$ (shown with dotted red line in the main panel). The areas shaded alternately in blue and red correspond to the energies of the emulated AE events.



Extended Data Figure 14: **Effect of thresholding on the emulated scaled aftershock rates in DDD simulations.** Aftershock rates r'_{as} after main shocks with different energies E'_{ms} scaled with $(E'_{ms})^{0.35}$. The panels correspond to rates observed at different thresholds $r'_{th,AE}$ used for the emulation of AE events: **a**, $r'_{th,AE} = 0.1$. **b**, $r'_{th,AE} = 1$. **c**, $r'_{th,AE} = 10$.

Quantity	length	stress	strain	time
Unit	$\rho^{-0.5}$	$Gb\rho^{0.5}$	$b\rho^{0.5}$	$(Gb^2M\rho)^{-1}$

Extended Data Table 1: **Units of the dimensionless quantities used in the simulations.**

Property	Earthquakes	Dislocation avalanches
Mechanism	Slip / crack	Dislocation movement
Expanse	in plane	in plane
Typical amplitude	m	nm
Typical reach	km	μm
Typical duration	minute – month	ms – s
Typical frequency	Hz	MHz
Size distribution	Gutenberg-Richter	Gutenberg-Richter
Aftershocks	Omori- and productivity law	Omori- and productivity law

Extended Data Table 2: **Comparison between earthquake and dislocation avalanche properties.**

570 **Supplementary information**

571 Link: <https://youtu.be/kAf4iP8PnkU>

572 Video 1: In situ SEM video of a compression of a $d = 8 \mu\text{m}$ micropillar
573 together with the measured force and the rate of AE events and released
574 AE energies. The ultrasonic AE signal recorded during the compression was
575 transformed into audible frequency domain that appears as a crackling noise.

576 Link: <https://youtu.be/XLLjSKhkWzA>

577 Video 2: Representative DDD simulation of $N = 1024$ dislocations subjected
578 to increasing shear stress with the protocol described in Methods. Dislocation
579 configuration is seen in top right panel. Red and blue colours refer to the sign
580 of the dislocations and the background colour with the colour scale represents
581 the internal shear stress generated by the dislocations. The force-time curve
582 is shown in the left panel together with the emulated AE count rate (see
583 Methods for details).

584 Link: https://youtu.be/Wb_ffzf2Cno

585 Video 3: Slowed down video of a representative plastic event (stress drop)
586 from Supplementary Video 2.

587 **References**

- 588 ¹Uchic, M. D., Dimiduk, D. M., Florando, J. N. & Nix, W. D. Sample
589 Dimensions Influence Strength and Crystal Plasticity. *Science* **305**, 986–
590 989 (2004).
- 591 ²Volkert, C. A. & Lilleodden, E. T. Size effects in the deformation of sub-
592 micron au columns. *Philos. Mag.* **86**, 5567–5579 (2006).
- 593 ³Miguel, M.-C., Vespignani, A., Zapperi, S., Weiss, J. & Grasso, J.-R. Inter-
594 mittent dislocation flow in viscoplastic deformation. *Nature* **410**, 667–671
595 (2001).
- 596 ⁴Weiss, J. & Marsan, D. Three-dimensional mapping of dislocation
597 avalanches: clustering and space/time coupling. *Science* **299**, 89–92
598 (2003).
- 599 ⁵Dimiduk, D. M., Woodward, C., LeSar, R. & Uchic, M. D. Scale-free
600 intermittent flow in crystal plasticity. *Science* **312**, 1188–1190 (2006).
- 601 ⁶Csikor, F. F., Motz, C., Weygand, D., Zaiser, M. & Zapperi, S. Disloca-
602 tion avalanches, strain bursts, and the problem of plastic forming at the
603 micrometer scale. *Science* **318**, 251–254 (2007).
- 604 ⁷Orowan, E. Zur kristallplastizität. iii. *Z. Phys.* **89**, 634–659 (1934).
- 605 ⁸Polanyi, M. Über eine art gitterstörung, die einen kristall plastisch machen
606 könnte. *Z. Phys.* **89**, 660–664 (1934).
- 607 ⁹Taylor, G. I. The mechanism of plastic deformation of crystals. part
608 i.—theoretical. *P. R. Soc. London* **145**, 362–387 (1934).

- 609 ¹⁰ Scruby, C. B. An introduction to acoustic emission. *J. Phys. E* **20**, 946
610 (1987).
- 611 ¹¹ Weiss, J. *et al.* Evidence for universal intermittent crystal plasticity from
612 acoustic emission and high-resolution extensometry experiments. *Phys.*
613 *Rev. B* **76**, 224110 (2007).
- 614 ¹² Gutenberg, B. & Richter, C. F. Magnitude and energy of earthquakes.
615 *Ann. Geofis.* **9** (1956).
- 616 ¹³ Utsu, T. Representation and Analysis of the Earthquake Size Distribution:
617 A Historical Review and Some New Approaches. *Pure Appl. Geophys.* **155**,
618 509–535 (1999).
- 619 ¹⁴ Utsu, T., Ogata, Y. & Matsu'ura, R. S. The Centenary of the Omori
620 Formula for a Decay Law of Aftershock Activity. *J. Phys. Earth* **43**, 1–33
621 (1995).
- 622 ¹⁵ Guglielmi, A. V. Interpretation of the Omori law. *Izv., Phys. Solid Earth*
623 **52**, 785–786 (2016).
- 624 ¹⁶ Helmstetter, A. Is earthquake triggering driven by small earthquakes?
625 *Phys. Rev. Lett.* **91**, 058501 (2003).
- 626 ¹⁷ Baró, J. *et al.* Statistical Similarity between the Compression of a Porous
627 Material and Earthquakes. *Phys. Rev. Lett.* **110**, 088702 (2013).
- 628 ¹⁸ Meng, F., Wong, L. N. Y. & Zhou, H. Power law relations in earthquakes
629 from microscopic to macroscopic scales. *Sci. Rep.* **9**, 10705 (2019).

- 630 ¹⁹ Jones, L. M. & Molnar, P. Some characteristics of foreshocks and their pos-
631 sible relationship to earthquake prediction and premonitory slip on faults.
632 *J. Geophys. Res.-Sol. Ea.* **84**, 3596–3608 (1979).
- 633 ²⁰ Bak, P., Christensen, K., Danon, L. & Scanlon, T. Unified scaling law for
634 earthquakes. *Phys. Rev. Lett.* **88**, 178501 (2002).
- 635 ²¹ Karsai, M., Kaski, K., Barabási, A.-L. & Kertész, J. Universal features of
636 correlated bursty behaviour. *Sci. Rep.* **2**, 1–7 (2012).
- 637 ²² Corral, A. Long-term clustering, scaling, and universality in the temporal
638 occurrence of earthquakes. *Phys. Rev. Lett.* **92**, 108501 (2004).
- 639 ²³ Ispánovity, P. D. *et al.* Avalanches in 2d dislocation systems: Plastic
640 yielding is not depinning. *Phys. Rev. Lett.* **112**, 235501 (2014).
- 641 ²⁴ Csikor, F. F., Zaiser, M., Ispánovity, P. D. & Groma, I. The role of density
642 fluctuations in the relaxation of random dislocation systems. *J. Stat. Mech.*
643 **2009**, P03036 (2009).
- 644 ²⁵ Zaiser, M. & Sandfeld, S. Scaling properties of dislocation simulations in
645 the similitude regime. *Model. Simul. Mater. Sci.* **22**, 065012 (2014).
- 646 ²⁶ Lehtinen, A., Costantini, G., Alava, M. J., Zapperi, S. & Laurson, L.
647 Glassy features of crystal plasticity. *Phys. Rev. B* **94**, 064101 (2016).
- 648 ²⁷ Sethna, J. P., Dahmen, K. A. & Myers, C. R. Crackling noise. *Nature*
649 **410**, 242–250 (2001).
- 650 ²⁸ Weiss, J. *et al.* From mild to wild fluctuations in crystal plasticity. *Phys.*
651 *Rev. Lett.* **114**, 105504 (2015).

- 652 ²⁹ Alcalá, J. *et al.* Statistics of dislocation avalanches in fcc and bcc metals:
653 dislocation mechanisms and mean swept distances across microsample sizes
654 and temperatures. *Sci. Rep.* **10**, 1–14 (2020).
- 655 ³⁰ Uchic, M., Shade, P. & Dimiduk, D. Plasticity of micrometer-scale single
656 crystals in compression. *Annu. Rev. Mater. Res.* **39**, 361–386 (2009).
- 657 ³¹ Britton, T. B. & Wilkinson, A. J. High resolution electron backscatter
658 diffraction measurements of elastic strain variations in the presence of
659 larger lattice rotations. *Ultramicroscopy* **114**, 82–95 (2012).
- 660 ³² Groma, I. & Székely, F. Analysis of the asymptotic properties of x-ray line
661 broadening caused by dislocations. *J. Appl. Cryst.* **33**, 1329–1334 (2000).
- 662 ³³ Borbély, A. & Groma, I. Variance method for the evaluation of particle
663 size and dislocation density from X-ray Bragg peaks. *Appl. Phys. Lett.* **79**,
664 1772–1174 (2001).
- 665 ³⁴ Hegyi, A. I. *et al.* Micron-scale deformation: A coupled in situ study of
666 strain bursts and acoustic emission. *Microsc. Microanal.* **23**, 1076–1081
667 (2017).
- 668 ³⁵ Kalácska, S. *et al.* Investigation of geometrically necessary dislocation
669 structures in compressed cu micropillars by 3-dimensional hr-ebstd. *Mat.*
670 *Sci. Eng. A.* **770**, 138499 (2020).
- 671 ³⁶ Bradski, G. The OpenCV Library. *Dr. Dobb's J.* **25**, 120–125 (2000).
- 672 ³⁷ Virtanen, P. *et al.* SciPy 1.0: Fundamental Algorithms for Scientific Com-
673 puting in Python. *Nat. Methods* **17**, 261–272 (2020).

- 674 ³⁸Heiple, C. R. & Carpenter, S. H. Acoustic emission produced by defor-
675 mation of metals and alloys - A review. *J. Acoustic Emission* **6**, 177–237
676 (1987).
- 677 ³⁹Jordi, B. *et al.* Experimental evidence of accelerated seismic release without
678 critical failure in acoustic emissions of compressed nanoporous materials.
679 *Phys. Rev. Lett.* **120**, 245501 (2018).
- 680 ⁴⁰Vu, C. C., & Weiss, J. Assymmetric damage avalanche shape in quasibrittle
681 materials and subavalanche (aftershock) clusters. *Phys. Rev. Lett.* **125**,
682 105502 (2020).
- 683 ⁴¹Hirth, J. P. & Lothe, J. *Theory of Dislocations* (John Willey & Sons, New
684 York, 1982), 2nd edn.
- 685 ⁴²Bakó, B., Groma, I., Györgyi, G. & Zimányi, G. Dislocation patterning:
686 The role of climb in meso-scale simulations. *Comp. Mater. Sci.* **38**, 22–28
687 (2006).
- 688 ⁴³Péterffy, G. & Ispánovity, P. D. An efficient implicit time integration
689 method for discrete dislocation dynamics. *Model. Simul. Mater. Sci.* **28**,
690 035013 (2020).
- 691 ⁴⁴Harris, C. R. *et al.* Array programming with NumPy. *Nature* **585**, 357–362
692 (2020).